

- shown after systemic treatment with MPTP [M. Filion, L. Tremblay, P. I. Bedard, *Brain Res.* **444**, 165 (1988); D. S. Rothblat and J. S. Schneider, *J. Neurosci.* **13**, 4372 (1993)].
43. Y. Kawaguchi, *J. Neurophysiol.* **67**, 1669 (1992); *J. Neurosci.* **13**, 4908 (1993).
44. Because most projection neurons are nearly silent except in highly context dependent circumstances (16, 17), it is extremely difficult to test directly the effects of TAN activity on projection neurons during behavioral tasks.
45. P. T. Akins, D. J. Surmeier, S. T. Kitai, *Nature* **344**, 240 (1990).
46. J. Hertz, A. Krogh, R. G. Palmer, *Introduction to the Theory of Neural Computation* (Addison-Wesley, Redwood City, CA, 1991).
47. The change in TAN activity could sharpen already fairly well synchronized activity in inputs from the

cortex or thalamus or could have maximum effect when the inputs to TANs and to TAN targets are contemporaneous.

48. H. V. S. Peeke and M. J. Herz, *Science* **173**, 80 (1971); M. Mishkin, B. Malamut, J. Bachevalier, in *Neurobiology of Human Learning and Memory*, G. Lynch, J. L. McGaugh, N. M. Weinberger, Eds. (Guilford, New York, 1984), pp. 65–77; D. Cook and R. P. Kesner, *Behav. Neural Biol.* **49**, 332 (1988); J. A. Saint-Cyr, A. E. Taylor, A. E. Lang, *Brain* **111**, 941 (1988); R. J. McDonald and N. M. White, *Behav. Neurosci.* **107**, 3 (1993).
49. The dopaminergic substantia nigra pars compacta has also been implicated in memory and learning in behavioral studies [A. Routtenberg and N. Holzman, *Science* **181**, 83 (1973); A. R. Cools, *Behav. Brain Res.* **1**, 361 (1980); M. G. Packard and N. M. White, *Behav. Neurosci.* **105**, 295 (1991)].

50. O. Hornykiewicz, in *Biochemistry and Pharmacology of the Basal Ganglia*, E. Costa, L. J. Coté, M. D. Yahr, Eds. (Raven, New York, 1966), pp. 171–185; O. Lindvall et al., *Science* **247**, 574 (1990).
51. H. Klawans, C. Goetz, C. Tanner, Eds., *Textbook of Clinical Neuropharmacology and Therapeutics* (Raven, New York, 1992).
52. P. Calabresi, R. Maj, A. Pisani, N. B. Mercuri, G. Bernardi, *J. Neurosci.* **12**, 4224 (1992); P. Calabresi, R. Maj, N. B. Mercuri, G. Bernardi, *Neurosci. Lett.* **142**, 95 (1992).
53. Supported by Javits Award, NIH grants NS25529 and NEI 02866, the Human Frontier Science Program, and Japanese ESC grant 03NP0101. We thank M. Anderson and S. Nelson for comments on the manuscript, C. Schneider for typing of the manuscript, G. Holm and H. Hall for technical support, and M. Johnson, who produced the image in Fig. 5.

RESEARCH ARTICLE

The “Ozone Deficit” Problem: $O_2(X, v \geq 26) + O(^3P)$ from 226-nm Ozone Photodissociation

R. L. Miller, A. G. Suits, P. L. Houston, R. Toumi,* J. A. Mack, A. M. Wodtke

Highly vibrationally excited $O_2(X^3\Sigma_g^-, v \geq 26)$ has been observed from the photodissociation of ozone (O_3), and the quantum yield for this reaction has been determined for excitation at 226 nanometers. This observation may help to address the “ozone deficit” problem, or why the previously predicted stratospheric O_3 concentration is less than that observed. Recent kinetic studies have suggested that $O_2(X^3\Sigma_g^-, v \geq 26)$ can react rapidly with O_2 to form $O_3 + O$ and have led to speculation that, if produced in the photodissociation of O_3 , this species might be involved in resolving the discrepancy. The sequence $O_3 + h\nu \rightarrow O_2(X^3\Sigma_g^-, v \geq 26) + O$; $O_2(X^3\Sigma_g^-, v \geq 26) + O_2 \rightarrow O_3 + O$ (where $h\nu$ is a photon) would be an autocatalytic mechanism for production of odd oxygen. A two-dimensional atmospheric model has been used to evaluate the importance of this new mechanism. The new mechanism can completely account for the tropical O_3 deficit at an altitude of 43 kilometers, but it does not completely account for the deficit at higher altitudes. The mechanism also provides for isotopic fractionation and may contribute to an explanation for the anomalously high concentration of heavy O_3 in the stratosphere.

Attempts to predict the stratospheric O_3 concentration date historically to Chapman's pioneering work in 1930 (1). Despite years of effort, there is still a significant discrepancy between the predicted and measured O_3 concentration in the upper stratosphere (2). It has recently been proposed that if the O_2 produced in O_3 photolysis were sufficiently vibrationally excited to react with ground-state O_2 to form O_3

+ O, this sequence of reactions might provide a means for formation of stratospheric O_3 (3–5). The work described here demonstrates that highly vibrationally excited O_2 is indeed formed in the photodissociation of O_3 . The quantum yield of this reaction has been determined so that the importance of the mechanism proposed in (3–5) can be evaluated. Calculations show that the inclusion of highly vibrationally excited O_2 in atmospheric models may help resolve the long-standing O_3 deficit problem. In addition, the new dissociation mechanism involving vibrationally excited O_2 may also be involved in resolving the long-standing mystery of why heavy isotopes of O_3 are more abundant in the stratosphere (6).

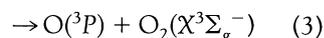
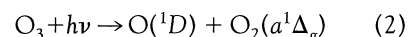
Two new experiments were performed to explore the photodissociation of O_3 at

wavelengths near 226 nm. The newly developed technique of photofragment imaging has been used to measure the velocity distribution of the $O(^3P)$ product; conservation of energy and momentum provide the internal energy of the O_2 sibling fragment. In addition, laser-induced fluorescence (LIF) on the Schumann-Runge bands has been performed to determine the distribution of $O_2(X^3\Sigma_g^-, v)$ population in the vibrational levels between $v = 19$ and $v = 26$. The experiments taken together indicate that the vibrational distribution of the $O_2(X^3\Sigma_g^-, v)$ produced at this dissociation wavelength is markedly bimodal, with one peak near $v = 14$ and another at $v = 27$.

The chemistry of O_3 has come under increasing scrutiny largely because of concern about stratospheric O_3 loss due to human activity. Production of stratospheric O_3 is believed to be due solely to reaction 1:



(where h is Planck's constant), which then rapidly generates O_3 in excess O_2 through three-body recombination: $O + O_2 + M \rightarrow O_3 + M$ ($M = O_2$ or N_2). Decomposition of O_3 is due to two photochemical pathways:



as well as to three catalytic processes commonly referred to as the HO_x , NO_x , and ClO_x cycles (7). Notwithstanding the large number of previous attempts (8–23), models of stratospheric chemistry underestimate the concentration of O_3 when compared to observations at altitudes between 35 and 80 km (2, 24, 25). This discrepancy is particularly puzzling because O_3 is in photochemical steady-state during daylight hours at these altitudes and its abundance is controlled by such a small number of well-studied chemical and photochemical reactions.

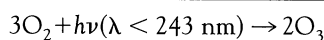
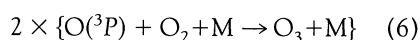
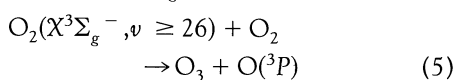
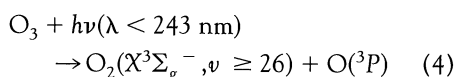
There have been at least two notable attempts to explain the so-called “ozone deficit” problem, each hypothesizing a sec-

R. L. Miller, A. G. Suits, and P. L. Houston are with the Department of Chemistry, Cornell University, Ithaca, NY, USA 14853–1301. R. Toumi is with the Centre for Atmospheric Science, Department of Chemistry, Lensfield Road, Cambridge CB2 1EW, United Kingdom. J. A. Mack and A. M. Wodtke are with the Department of Chemistry, University of California, Santa Barbara, CA, USA 93106.

*Present address: Department of Physics, Imperial College, London SW7 2BZ, United Kingdom.

ond O₃ formation channel in addition to reaction 1. First, it was suggested that O₂(*a*¹Δ_g) produced in reaction 2 could absorb radiation in the A'³Δ_u ← *a*¹Δ_g continuum and dissociate to yield two oxygen atoms, each of which would immediately form O₃ in excess O₂ (26). The hypothesis was abandoned when it was determined that this absorption system is far too weak to dissociate O₂ effectively (27, 28). Second, it was suggested that reaction 3 might produce O₂(X³Σ_g⁻) in sufficiently high vibrational levels to be dissociated by sunlight (λ > 300 nm); again, the resulting two O atoms would each yield an O₃ molecule in excess O₂ (29). Although vibrationally excited O₂ is produced from reaction 3 (29, 30) and despite the fact that initial atmospheric modeling appeared promising (31, 32), this mechanism was abandoned when measurements showed that collisional relaxation of vibrationally excited O₂ was much faster than its solar photodissociation (4, 30).

A third hypothesis has recently been suggested as the result of stimulated emission pumping experiments on highly vibrationally excited O₂(X³Σ_g⁻, *v* ≫ 0). These experiments revealed the possibility that O₂(X³Σ_g⁻, *v* ≥ 26) can react directly with O₂ to form O₃ + O, suggesting the third possible mechanism (4):

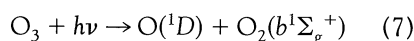


In addition to observing a very sharp increase in the relaxation rate of O₂(*v*) by O₂ at *v* = 26, which is the threshold for reaction 5, Rogaski *et al.* demonstrated that the removal rate for O₂(*v* = 26) or O₂(*v* = 27) by O₂ is 25 or 150 times faster, respectively, than the relaxation rate of these species by N₂ (4).

The key to evaluating the significance of this mechanism is to determine the quantum yield for the production of O₂(X³Σ_g⁻, *v* ≥ 26), a quantity we denote $\Phi_{v \geq 26}(\lambda)$. This yield in turn is the product of two factors: a quantum yield that describes the probability of reaction 3, denoted $\Phi_3(\lambda)$, and the fraction that describes the probability for reaction 3 to produce such high vibrational states of O₂, denoted $R_{v \geq 26}(\lambda)$. Thus, $\Phi_{v \geq 26}(\lambda) = \Phi_3(\lambda)R_{v \geq 26}(\lambda)$.

Numerous studies of $\Phi_3(\lambda)$ have been carried out. It is generally agreed that reactions 2 and 3 dominate the photodissociation of O₃ at 248 nm and that the quantum yield for 2 is given by $\Phi_2(248 \text{ nm}) = 0.85$

to 0.90 so that $\Phi_3(248 \text{ nm}) = 0.15$ to 0.10 (33). The primary processes at wavelengths shorter than 248 nm have not been as thoroughly investigated. The most recent study concluded that: (i) $\Phi_2(222 \text{ nm}) = 0.87$; (ii) $\Phi_3(222 \text{ nm}) = 0.13$; (iii) $\Phi_{\text{O}(^1D)}(193 \text{ nm}) = 0.46$; (iv) $\Phi_{\text{O}(^3P)}(193 \text{ nm}) = 0.57$; and (v) $\Phi_{\text{O}_2}(b^1\Sigma_g^+)(193 \text{ nm}) = 0.50$ (23). From the similarity in yields for O(¹D) and O₂(*b*¹Σ_g⁺) it was inferred that at 193 nm a third O₃ dissociation pathway is possible:



with $\Phi_7(193 \text{ nm}) = 0.5$. These conclusions were all based solely on observation of the reactivity of O(³P) as a function of time after the photolysis of O₃.

In this article we present experimental evidence which shows that O₃ photolysis at 226 nm produces O₂(X³Σ_g⁻) with a bimodal vibrational distribution and a substantial yield of O₂(X³Σ_g⁻, *v* ≥ 26). The evidence consists of: (i) measurement of a bimodal O(³P) translational energy distribution with one peak at a translational energy release consistent with reaction 4 and (ii) direct spectroscopic observation that the relative population of O₂(X³Σ_g⁻, *v*) for *v* = 19 to *v* = 26 is also bimodal with a relative minimum in the population at *v* = 22. Comparison of the two results by considering conservation of energy and linear momentum shows that they are in good agreement. The two experiments taken together make a compelling case that O₃ photolysis at 226 nm results in a markedly bimodal vibrational distribution for the O₂(X³Σ_g⁻), with one peak at *v* = 14 and another at *v* = 27.

We also measured the value of $R_{v \geq 26}$ from which $\Phi_{v \geq 26}$ can be derived so that we can evaluate the mechanism suggested by reactions 4 to 6. Although the yield is small enough so that it would not have produced a noticeable effect in the experiments of Horowitz *et al.* (34), it can have an appreciable effect on stratospheric O₃ concentrations. A two-dimensional (2D) (altitude and latitude) atmospheric model was used which suggests that this mechanism may provide an explanation for the discrepancy between the measured and calculated O₃ concentrations in the stratosphere.

Experimental. Two independent experiments were carried out in order to determine the O₂(X³Σ_g⁻, *v*) vibrational distribution. These will be referred to hereafter as the "photofragment imaging" experiment and the "pump/probe" experiment.

The photofragment imaging apparatus has been described in detail elsewhere (35, 36). A 10 percent O₃-He mixture was formed into a collimated and skimmed pulsed molecular beam (37) and was then crossed at a right angle by the ultraviolet

(UV) output of a pulsed laser tuned near 226 nm (38). The tunable laser served both to dissociate the O₃ and to ionize the selected O(³P_{*j*}) fragment through 2+1 resonance enhanced multiphoton ionization (REMPI) that uses an O(3*p* ³P_{*j*} ←← 2*p* ³P_{*j*}) transition.

An electric field (~1000 V cm⁻¹) was applied to extract the ionized O(³P_{*j*}) fragments into a Wiley-McLaren time-of-flight (TOF) mass spectrometer (39) mounted so that the ion flight direction was perpendicular to the horizontal plane defined by the laser and molecular beam. The ions traveled upward through the field-free 0.5-m flight tube (TOF = 3.06 μs) and then struck a 2D position-sensitive detector that consists of a double-chevron microchannel plate assembly coupled to a fast phosphor screen. The image of the phosphor screen was recorded by a 512 pixel by 480 pixel charge-injection device camera electronically shuttered (1-μs gate width) to capture the signal corresponding to the mass of an O atom. A set of 256 images was accumulated by a real-time video averager with 16-bit resolution. The molecular beam valve was turned off and another set of 256 images was then summed to obtain background. The net signal minus background was accumulated until adequate image quality was obtained, typically after 5000 to 17,000 total laser shots (40).

The branching ratios for the fine-structure states of O(³P_{*j*}) were determined by placing a photomultiplier tube near the phosphor screen to collect all of the ion signal as the laser was tuned over the O(³P_{*j*}) resonances at laser wavelengths 226.23, 226.06, and 225.65 nm for *j* = 0, 1, and 2, respectively (41). The output was then sent to a boxcar averager gated at the appropriate arrival time. The laser power was also simultaneously measured with a photodiode in order to normalize the O(³P_{*j*}) signal intensity for shot-to-shot fluctuations in laser power.

In the pump/probe experiment, O₃ was swept from a temperature-controlled trap by dry N₂, and its partial pressure was determined by the attenuation of the 253.7-nm Hg resonance line (42) in an absorption cell placed in series with a 25-cm-long stainless steel photolysis cell within which the total pressure was measured by a capacitance manometer. Typical operating conditions used O₃ pressures of 30 to 50 mtorr in 100 torr N₂ flowing at 3.5 liters/min. The large excess of N₂ was required in order to quench the O(¹D) produced in reaction 2 rapidly, as discussed below. The O₃ was dissociated by a 20-ns-long pump pulse of 226-nm light (43). As in previous experiments (3, 4), vibrationally excited O₂ photoproducts were then probed at a variable time delay (2 μs typically) by LIF through the well-known B³Σ_u⁻ ← X³Σ_g⁻ Schu-

mann-Runge absorption system (44). The LIF signal was monitored at right angles to the overlapped pump and probe laser beams by a photomultiplier tube assembly (Hamamatsu R212) equipped with collection optics to enhance signal and with a filter (UG-11) to reduce scattered light. The PMT current was processed by a gated integrator and digitized for storage on a PC.

Results. A typical image obtained for the $O(^3P_2)$ fragment from the 226-nm photolysis of O_3 is shown in Fig. 1. The image is the 2D projection of the nascent 3D velocity distribution obtained for an alignment of the laser polarization vector vertical and parallel to the plane of the image. The ion intensity is represented by a continuous "heat" scale with white corresponding to the highest signal intensity.

An examination of the $O(^3P_2)$ image shows two pairs of symmetric lobes of intensity, each with a markedly anisotropic (nearly $\cos^2\theta$) (45) angular distribution about the polarization direction of the photolysis laser. The inner lobes correspond to low-velocity O atom fragments, whereas the outer lobes correspond to faster fragments. The observed $\cos^2\theta$ dependence in the intensity pattern is consistent with the fact that the Hartley band dissociation of O_3 is known to occur through a parallel transition followed by dissociation on a time scale rapid compared to O_3 rotation (12). However, observation of a bimodal O atom velocity distribution was unexpected.

Images similar to that shown in Fig. 1 were also obtained for the $O(^3P_1)$ and $O(^3P_0)$ fragments. These images demonstrate the same qualitative features as the $O(^3P_2)$ product, but the relative intensity of the inner lobes to the outer lobes gen-

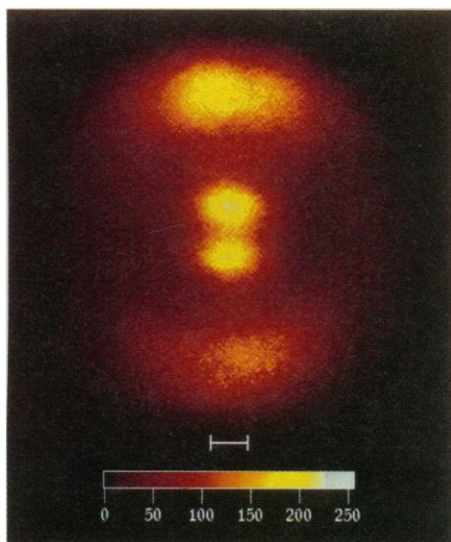


Fig. 1. The 2D projection of the 3D $O(^3P_2)$ velocity distribution produced after dissociation of O_3 at 226 nm. The length of the calibration bar represents 1000 m/s.

erally decreases as j decreases.

The procedure for reconstructing the 3D velocity distribution from the 2D spatial projection has been described in detail (46–50). The cylindrical symmetry of the velocities around the polarization axis of the laser coupled with the fact that the 2D projection is made perpendicular to this vector allows one to reconstruct the entire 3D velocity distribution by performing an inverse Abel transformation on the 2D image (50). The speed distribution of a fragment can then be determined by integrating its 3D velocity distribution over all angles at each speed (51). Many images were obtained for the 3P_2 , 3P_1 , and 3P_0 O atoms. For each $O(^3P_j)$ fragment, the individual images were analyzed to yield speed distributions, and these were then converted to translational energy distributions and averaged (52).

The smooth solid line in Fig. 2 shows the average in the center-of-mass frame of the translational energy distribution for formation of $O(^3P_j)$ from the 226-nm photolysis of O_3 [the dotted lines give error limits ($\pm 1\sigma$) and the points with error bars are discussed below]. This distribution was obtained by weighting the average total translational energy distributions calculated for the $O(^3P_2)$, $O(^3P_1)$,

and $O(^3P_0)$ photofragments by the experimentally determined branching ratios, $(5.4 \pm 0.4):(2.7 \pm 0.2):(1.0)$ for $O(^3P_j)$, $j = 2:1:0$, respectively. These branching ratios were determined from integrated REMPI signals corrected for laser power (53) and two-photon line strength (41).

The bimodal nature of the $O(^3P_2)$ image shown in Fig. 1 is preserved in the translational energy distribution displayed in Fig. 2. Two peaks are observed; a broad peak centered on an $O(^3P)$ velocity of ~ 4000 m s^{-1} (2 eV total translational energy release) that corresponds to the outer lobes observed in the image shown in Fig. 1, and a sharp peak centered on an $O(^3P)$ velocity of ~ 1050 m s^{-1} (0.14 eV total translational energy release) that corresponds to the inner lobes.

The broad peak at higher translational energy is consistent with reaction 3. The origin of the slower $O(^3P)$ fragments, however, must be examined carefully to ensure that it is the result of photochemical O_3 dissociation. Several alternative sources of the slow velocity peak in Fig. 1 have been considered and rejected: (i) The slow $O(^3P)$ fragments might result from the dissociation of O_3 clusters instead of the monomer. This

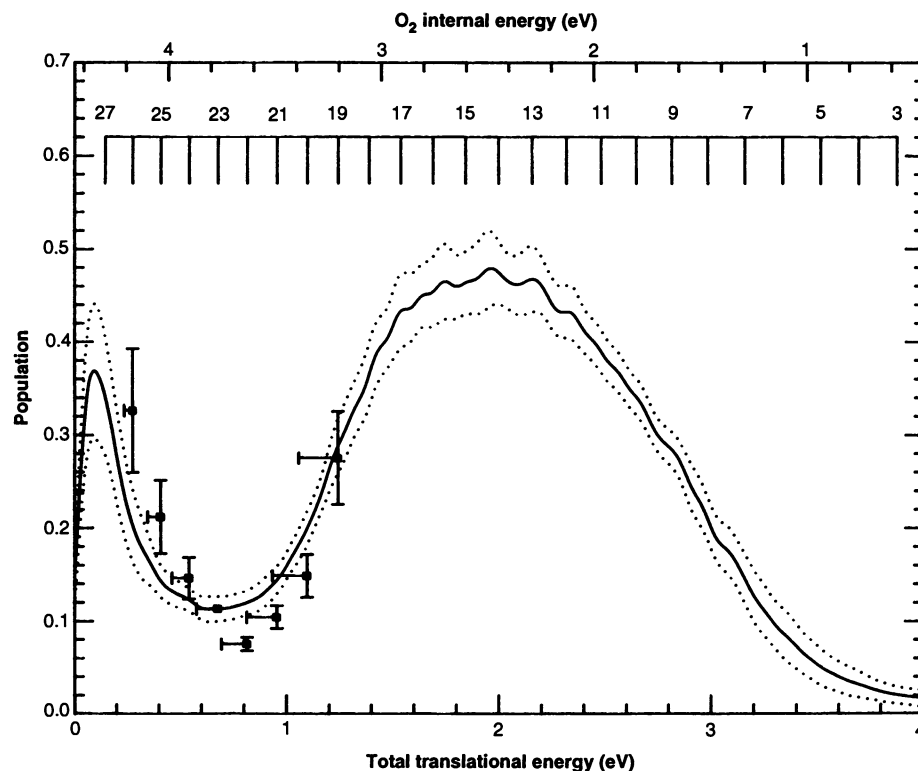


Fig. 2. The average translational distribution for the dissociation of O_3 to $O(^3P) + O_2(X^3\Sigma_g^-)$ at 226 nm. The bottom abscissa gives the translational energy, and the top abscissa gives the corresponding O_2 internal energy. The vibrational levels of O_2 are indicated from 3 to 27 on the comb. The smooth line gives the energy distribution derived from the photofragment imaging experiment, and the dotted lines give $\pm 1\sigma$ error limits. The points with error bars give the energy distribution derived from the pump/probe experiment. The probability for translational energy release corresponding to formation of $O_2(X^3\Sigma_g^-, v = 23)$ has been set equal in the two experiments. The agreement indicates that the O_2 internal energy is in vibration.

explanation was ruled out when the peak at 0.14 eV was observed with the same intensity for images obtained when a lower concentration (0.1 percent O₃-He) beam and a heated nozzle were used. (ii) The slow O(³P) fragments might result from the secondary dissociation of O₂ produced in the photolysis of O₃. Conservation of energy and momentum eliminate this possibility. (iii) The sharp peak might be due to the photolysis of residual O₂ in the O₃ trap (54). The O(³P) velocity distributions observed in these experiments, however, are too slow and broad to be explained by this hypothesis. (iv) The center spot in the O(³P) image might correspond to O atoms produced from the thermal decomposition of O₃ (22). The observed anisotropy of the center lobes eliminates this possibility. We thus conclude that the observed slow O(³P) fragments are indeed produced as a result of O₃ photodissociation.

The total energy available to the products, E_{avail} , is fixed by Eq. 8:

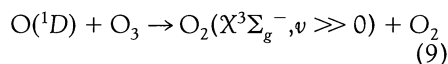
$$E_{\text{avail}} = E_{h\nu} - D_0[\text{O}_2 - \text{O}] = E_{\text{kinetic}} + E_{\text{internal}} \quad (8)$$

where $E_{h\nu}$ is the energy of the 226-nm photon, $D_0[\text{O}_2 - \text{O}]$ is the bond energy of O₃, and E_{kinetic} and E_{internal} are the kinetic and internal energy of the photoproducts, respectively. The internal energy is the sum of that for the O atom and that for the O₂, and the former is fixed because the laser wavelength ionizes a particular ³P_{*j*} component. Consequently, the bimodal E_{kinetic} evident in the image of Fig. 1 shows that O₂ is formed with a bimodal internal energy distribution.

Although the O atom imaging results can determine the amount of internal energy in the O₂ product, they cannot determine whether this energy is in vibrational or electronic degrees of freedom. The sharp peak at ~4.3 eV internal energy is consistent either with production of O₂(X³Σ_{*g*}⁻, *v* = 27) or with formation of electronically excited O₂(c¹Σ_{*u*}⁻, A³Σ_{*u*}⁺, or A¹Σ_{*u*}⁺) (55). Pump/probe experiments demonstrate that the internal energy is mostly in vibration.

Direct evidence for the production of O₂(X³Σ_{*g*}⁻, *v* = 26) can be seen in Fig. 3, which shows the (B³Σ_{*u*}⁻, *v*' = 2 ← X³Σ_{*g*}⁻, *v*'' = 26) LIF spectrum observed 2 μs after O₃ photolysis at 226 nm. Four of the six branches associated with this well-known triplet spectral system are clearly resolved and two are blended. Assignment of the spectral features is simplified by the previous work of Creek and Nichols (56) and is unambiguous. Similar spectra were recorded and assigned for the bands: (B³Σ_{*u*}⁻, *v*' = 2 ← X³Σ_{*g*}⁻, *v*'' = 26-19). The LIF signal was always found to be linear with the power of both the pump and probe lasers.

The pump/probe experiments were carried out in a large excess of N₂ in order to quench O(¹D) produced by O₃ photolysis and thereby inhibit the production of highly vibrationally excited O₂ through reaction 9:



The rate constant for reaction 9 is $2.4 \times 10^{-10} \text{ cm}^3 \text{ s}^{-1}$ (57), whereas that for the quenching of O(¹D) by N₂ is $2.6 \times 10^{-11} \text{ cm}^3 \text{ s}^{-1}$ (57). Thus, under our typical operating conditions of 100 torr of N₂ and 0.03 torr of O₃, less than 1 part in 300 of the O(¹D) undergoes reaction 9. These conditions, which have also been found to be effective in other studies (30), assure that the dominant process of O₂(X³Σ_{*g*}⁻, *v* >> 0) production is from the photolysis of O₃. The dominance was confirmed by determining the dependence of the O₂ LIF signal on O₃ partial pressure. The results of such a measurement for O₂(X³Σ_{*g*}⁻, *v* = 25) are shown in Fig. 4. The good linear fit to the data establishes that O₂(X³Σ_{*g*}⁻, *v* = 25) is not produced by reaction 2 followed by reaction 9, for which a quadratic pressure dependence would be expected.

The relative populations of O₂(X³Σ_{*g*}⁻, *v*'') produced in the 226-nm photolysis of

O₃ were determined by making comparative measurements of the LIF intensities from two adjacent vibronic bands, that is, by comparing B³Σ_{*u*}⁻, *v*' = 2 ← X³Σ_{*g*}⁻, *v*'' and B³Σ_{*u*}⁻, *v*' = 2 ← X³Σ_{*g*}⁻, *v*'' - 1, with *v*'' = 26-20, while maintaining constant experimental conditions. This process was repeated in a pairwise fashion down through the vibrational manifold (that is 26:25, 25:24, 24:23, and so forth) to give a relative population distribution for O₂(X³Σ_{*g*}⁻, *v*'' = 26-19) (Table 1).

In order to ensure that the LIF signal comparisons between adjacent vibrational states were valid in all cases, the LIF emission detected from the B-state in the O₂ Schumann-Runge transitions was always from the same vibrational level, *v*' = 2. In each comparison, the probe laser was scanned over the same number of P and R triplets for the respective vibronic bands and the integrated LIF signal was derived. This procedure simultaneously eliminates the influence of laser linewidth and Hönl-London factors. The resulting integrated LIF signal needed to be corrected only for relative laser power and for differences in the Franck-Condon factors. The Franck-Condon factors were calculated with an RKR program and agree quite well with

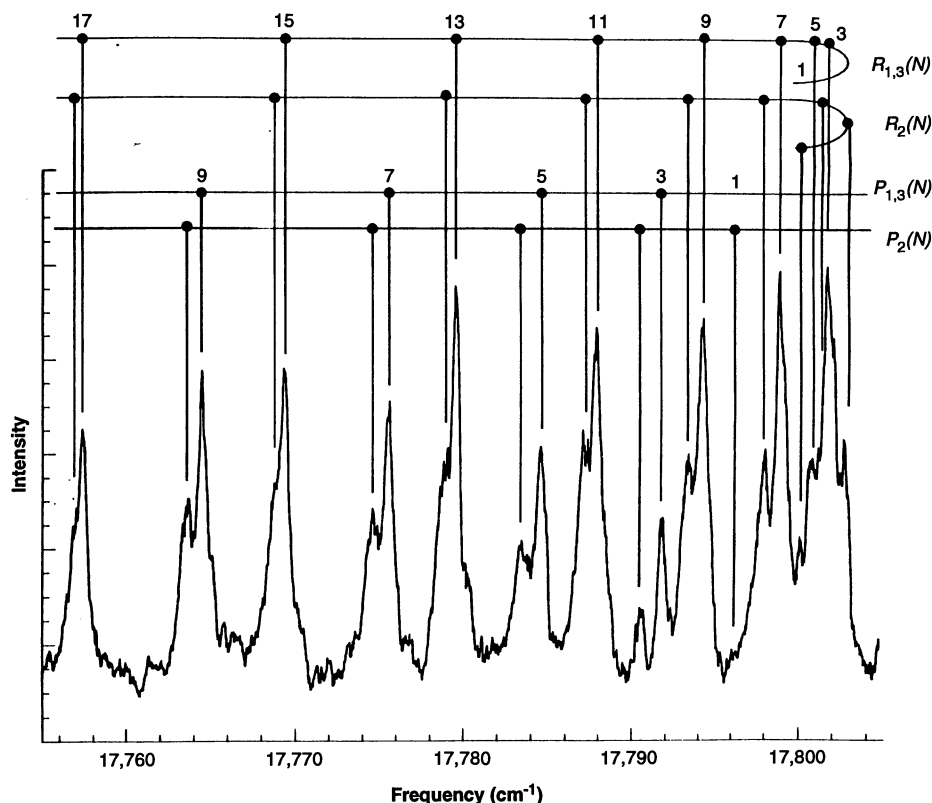


Fig. 3. The LIF spectrum of O₂(X³Σ_{*g*}⁻, *v* = 26). The observed transitions belong to the B³Σ_{*u*}⁻, *v*' = 2 ← X³Σ_{*g*}⁻, *v*'' = 26 vibronic band of the Schumann-Runge electronic system. P and R denote Δ*N* = -1 and +1, respectively. The subscripts 1, 2, and 3 indicate the three spin components of the spectrum, where *J* = *N* + 1, *J* = *N*, and *J* = *N* - 1, respectively. All labeled transitions are for Δ*J* = Δ*N*. This spectrum was observed 2 μs after the pump laser was fired. The rotational structure is collisionally equilibrated but vibrational relaxation has not yet set in.

reported values (58).

The influence of collisional relaxation on the nascent vibrational population distribution was evaluated by monitoring the time dependence of the LIF signal for each vibrational state. The LIF signal obtained at 2- μ s delay was not measurably different than the value back-extrapolated to zero time delay in any of the measurements. The rate constants for $O_2(X^3\Sigma_g^-, v)$ relaxation by O_3 have been shown to be on the order of $1 \times 10^{-11} \text{ cm}^3 \text{ s}^{-1}$ (59). The rate constants for relaxation by N_2 have also been previously measured (4, 30, 60). The collisional lifetimes observed in the pump/probe experiment were consistent with relaxation by a mixture of O_3 and N_2 .

Evidence for the $O_2(X^3\Sigma_g^-, v \geq 26) + O(^3P)$ product channel. A comparison of the photofragment imaging and pump/probe results provides compelling evidence for the $O_2(X^3\Sigma_g^-, v \geq 26) + O(^3P)$ product channel. The bimodal translational energy distribution shown in Fig. 2 is proof of a bimodal internal energy distribution in the O_2 photoproduct, but it is not clear from this distribution alone whether the internal energy is electronic or vibrational.

The relative vibrational distribution derived from the pump/probe experiment (Ta-

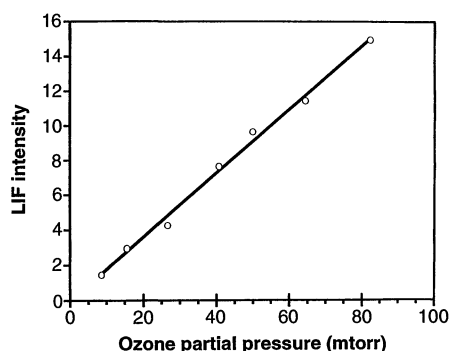


Fig. 4. The LIF signal dependence on O_3 partial pressure. The LIF intensity of the $^3\Sigma_u^-, v' = 2 \leftarrow X^3\Sigma_g^-, v'' = 25$ vibronic band is shown as a function of O_3 partial pressure. If the signal is due to one-photon dissociation of O_3 , a linear dependence is expected. If the signal were due to reaction 2 followed by reaction 9, a quadratic dependence would be found.

Table 1. Derived population ratios and relative population distribution of $O_2(X^3\Sigma_g^-, v'')$ from the 226-nm photodissociation of O_3 .

Population ratio	$v'':v'' - 1$	Relative population	v''
$(1.54 \pm 0.13):1.0$	26:25	1.0	26
$(1.45 \pm 0.15):1.0$	25:24	0.65	25
$(1.29 \pm 0.20):1.0$	24:23	0.45	24
$(1.51 \pm 0.15):1.0$	23:22	0.35	23
$(0.72 \pm 0.05):1.0$	22:21	0.23	22
$(0.70 \pm 0.07):1.0$	21:20	0.32	21
$(0.54 \pm 0.05):1.0$	20:19	0.46	20
		0.85	19

ble 1) can be used to predict the shape of the kinetic energy distribution of Fig. 2 in the range from 0.2 to 1.5 eV translational energy release. If a kinetic energy distribution derived in this way were to agree well with the kinetic energy distribution of Fig. 2, it would be strong evidence for a bimodal vibrational energy distribution in the O_2 photoproduct. The results of such an analysis are shown as points with error bars in Fig. 2. The probability for translational energy release corresponding to formation of $O_2(X^3\Sigma_g^-, v = 23)$ has been set equal in the two experiments, and the horizontal error bars are indicated for assignment of 0 to 15 percent of the remaining available energy to rotation, in agreement with previous investigations of the lower vibrational levels (61). The very good agreement between the two experiments is evidence that $O_2(X^3\Sigma_g^-, v)$ is produced in a bimodal vibrational distribution when O_3 is photolyzed at 226 nm (62).

The translational energy distribution determined from the photofragment imaging experiments can be used to determine the quantum yield for production of $O_2(X^3\Sigma_g^-, v \geq 26)$, $\Phi_{v \geq 26}(\lambda = 226 \text{ nm})$. Recall that this quantum yield is the product of two factors: $\Phi_{v \geq 26}(\lambda = 226 \text{ nm}) = \Phi_3(\lambda = 226 \text{ nm})R_{v \geq 26}(\lambda = 226 \text{ nm})$. The value of $R_{v \geq 26}(\lambda = 226 \text{ nm})$ can be determined by integrating the curve in Fig. 2 from 0 to 0.275 eV and dividing this by the total area under the curve. The result is $R_{v \geq 26}(\lambda = 226 \text{ nm}) = 0.081 \pm 0.015$. For the reported value $\Phi_3(\lambda = 222 \text{ nm}) = 0.13$, the value of $\Phi_{v \geq 26}(\lambda = 226 \text{ nm})$ is calculated to be 0.011 and is large enough to have an impact on the stratospheric O_3 budget (4), as we discuss below.

Possible effect on the stratospheric O_3 concentration. Our observation that $O_2(X^3\Sigma_g^-, v \geq 26)$ is produced in the photodissociation of O_3 allows us to evaluate the importance of the mechanism of reactions 4, 5, and 6 on the stratospheric O_3 concentration. Two calculations are performed, a steady-state evaluation of the increase in O_3 production rate and a model calculation that includes radiative, transpore, and chemical effects. The steady-state

calculation helps show the principles and assumptions involved in the computer model and is presented for clarity.

We start by calculating the steady-state concentration of $O_2(X^3\Sigma_g^-, v \geq 26)$ produced by the photolysis of O_3 . Let $\Phi_{v \geq 26}$ be the overall quantum yield for $O_2(X^3\Sigma_g^-, v \geq 26)$ formation from O_3 photodissociation, and let k_D be the total collisional removal rate constant for $O_2(X^3\Sigma_g^-, v \geq 26)$. In the steady-state assumption (t is time):

$$\begin{aligned} \frac{d[O_2(v)]}{dt} &= 0 \\ &= [O_3] \int_{\lambda < 243 \text{ nm}} J_{O_3}(\lambda, z, \chi) \Phi_{v \geq 26}(\lambda) d\lambda \\ &\quad - k_D [O_2(v)] [O_2] \end{aligned} \quad (10)$$

where $J_{O_3}(\lambda, z, \chi)$ is the photodissociation coefficient of O_3 , which depends on wavelength (λ), altitude (z), and zenith angle (χ). $O_2(v)$ is an abbreviation for $O_2(X^3\Sigma_g^-, v \geq 26)$, and we have assumed that O_2 is principally responsible for the collisional removal of $O_2(v)$. The spectral region over which production of $O_2(X^3\Sigma_g^-, v \geq 26)$ is allowed is limited on the long-wavelength end by its energetic threshold at 243 nm and on the short-wavelength end by absorption of light in the O_2 Schumann-Runge bands at ~ 190 nm. The concentration of $O_2(X^3\Sigma_g^-, v \geq 26)$ can be found within the steady-state approximation and is shown in Eq. 11:

$$\begin{aligned} [O_2(v)] &= \frac{[O_3] \int_{\lambda < 243 \text{ nm}} J_{O_3}(\lambda, z, \chi) \Phi_{v \geq 26}(\lambda) d\lambda}{k_D [O_2]} \end{aligned} \quad (11)$$

Let the reaction rate constant for $5, O_2(v) + O_2 \rightarrow O_3 + O(^3P)$, be k_5 so that the branching ratio to these products is k_5/k_D . The additional O_3 production rate due to reaction 5 is then given by Eq. 12:

$$\begin{aligned} \frac{d[O_3]}{dt} &= 2k_5 [O_2] [O_2(v)] \\ &= 2k_5 [O_2] \\ &\quad \frac{[O_3] \int_{\lambda < 243 \text{ nm}} J_{O_3}(\lambda, z, \chi) \Phi_{v \geq 26}(\lambda) d\lambda}{k_D [O_2]} \\ &= 2 \frac{k_5}{k_D} [O_3] \int_{\lambda < 243 \text{ nm}} J_{O_3}(\lambda, z, \chi) \Phi_{v \geq 26}(\lambda) d\lambda \end{aligned} \quad (12)$$

The leading factor of 2 comes from the assumption that the O atom produced in

reaction 5 will rapidly recombine with O₂ to form O₃.

Because the rate of O₃ production in the conventional mechanism is 2J_{O₂}[O₂] (63), the fractional additional odd oxygen production, *F*, relative to that provided by O₂ dissociation is given by Eq. 13:

$$F = \frac{k_5}{k_D} \frac{[\text{O}_3] \int_{\lambda < 243 \text{ nm}} J_{\text{O}_3}(\lambda, z, \chi) \Phi_{v \geq 26}(\lambda) d\lambda}{J_{\text{O}_2}[\text{O}_2]} \quad (13)$$

Because wavelength-dependent data are not available, we assume that $\Phi_{v \geq 26}(\lambda) = \Phi_{v \geq 26}(\lambda = 226 \text{ nm})$ and that this yield is constant over the integrated wavelength interval. Thus, Eq. 13 can be simplified:

$$F = \frac{k_5}{k_D} \frac{[\text{O}_3] \Phi_{v \geq 26}(\lambda = 226 \text{ nm}) \int_{\lambda < 243 \text{ nm}} J_{\text{O}_3}(\lambda, z, \chi) d\lambda}{J_{\text{O}_2}[\text{O}_2]} \quad (14)$$

We can further define *R*₂₄₃ as the fraction of O₃ photolysis taking place at wavelengths shorter than 243 nm:

$$R_{243} = \frac{\int_{\lambda < 243 \text{ nm}} J_{\text{O}_3}(\lambda, z, \chi) d\lambda}{\int J_{\text{O}_3}(\lambda, z, \chi) d\lambda} \quad (15)$$

From Eq. 15 and recalling that $\Phi_{v \geq 26}(\lambda) = \Phi_3 R_{v \geq 26}$, we can rewrite Eq. 14 as:

$$F = \frac{k_5}{k_D} [\text{O}_3] \Phi_3 R_{v \geq 26} \frac{R_{243} \int J_{\text{O}_3}(\lambda, z, \chi) d\lambda}{J_{\text{O}_2}[\text{O}_2]} \quad (16)$$

$$= \frac{k_5}{k_D} R_{243} R_{v \geq 26} \frac{J_{\text{O}_3 \rightarrow ^3\text{P}}[\text{O}_3]}{J_{\text{O}_2}[\text{O}_2]}$$

where $J_{\text{O}_3 \rightarrow ^3\text{P}} \equiv \Phi_3 \int J_{\text{O}_3}(\lambda, z, \chi) d\lambda$ is obtained from (2) and is the total O₃ photolysis rate constant leading to O(³P₁).

We can now estimate *F*. For this calculation we take *R*_{v ≥ 26} = 0.081 as discussed

above. We further assume that *k*₅/*k*_D is unity. This assumption is supported by recent experiments from the Santa Barbara group (J.A.M. and A.M.W.) which show that only about 1 percent of O₂ prepared in *v* = 27 appears at a later time in *v* = 26. We can approximate *R*₂₄₃, defined in Eq. 15, as being equal to *R*₂₄₀, defined similarly and reported in (64). Table 2 shows the results of this analysis for altitudes from 40 to 55 km, where the next-to-last column gives the resulting values of *F*. Table 2 shows that the proposed new source produces odd oxygen at a rate between 14 and 48 percent of the principle O₂ photodissociation source.

These additional production rates will not result in comparable percentage increases in the steady-state O₃ concentration, because the rate-limiting step in all of the catalytic destruction cycles involves a reaction with O atoms, and this species will have a larger concentration with the new mechanism. However, the steady-state calculations suggest that a more thorough treatment of the atmospheric modeling is warranted.

Therefore, we have included this new mechanism in a radiative-transport-chemical 2D (altitude and latitude) computer model that includes both production and loss processes (65). We assume in this model that the triplet quantum yield at wavelengths less than 243 nm is $\Phi_3 = 0.13$ (23) and that *R*_{v ≥ 26} at these wavelengths is equal to its measured value at $\lambda = 226 \text{ nm}$, namely *R*_{v ≥ 26} = 0.081. We also assume that all O₂(X³Σ_g⁻, *v* ≥ 26) formed in O₃ photolysis leads to O₃ + O. The model uses the solar flux and its absorption by O₂ and O₃ to generate the wavelength-dependent radiation flux at any given altitude and latitude. The resulting flux is used to calculate the molecular concentrations, but because these concentrations influence the flux, the calculation must be performed in a self-consistent manner until convergence is reached. Convergence is typically reached in a few model time steps.

The increase in O₃ calculated by the model over that calculated without the new dissociation mechanism is shown in Fig. 5. Maximum increases of nearly 10 percent are observed in the tropical upper stratosphere near 2 hPa (about 43 km) (66). Above this

region, the calculated increase is less because [O₃] decreases. At lower altitudes, the optical depth increases and the O₃ photolysis coefficient is smaller. Below 10 hPa (about 30 km), there is actually a decrease in O₃ by about 0.7 percent. This decrease is a consequence of the increased O₃ in the upper stratosphere which increases the optical depth and reduces the O₂ photolysis in the lower stratosphere. The photochemical lifetime of O₃ in the tropical lower stratosphere is sufficiently short (months) to respond to changes in chemical production. Overall, the total tropical O₃ column increases by 1 percent. At high latitudes, the mechanism is less effective because the optical depth is larger. The reduced efficiency at high latitudes contrasts with the previous mechanism, which depended on the photolysis of vibrationally excited O₂ at longer wavelengths, leading to significant increases at high latitudes (30).

The results of the model calculations presented here are consistent with recent analysis by Eluszkiewicz and Allen, who concluded that the O₃ deficit was largest at low latitudes (2). Near 1 hPa they calculate an O₃ deficit of about 8 percent (see their figure 9a), so that the 10 percent increase predicted by the new mechanism almost exactly accounts for the deficit. However, near 0.4 hPa where the new mechanism increases O₃ by ~2.5 percent the calculated deficit is as high as 20 percent. Nevertheless a substantial part of the global O₃ deficit may now be accounted for. Refinements to the model, such as a wavelength dependence for Φ_3 or *R*_{v ≥ 26}, might improve the agreement, but such adjustments seem premature in advance of experimental measurements.

Possible effect on heavy O₃ distribution. The concentration of heavy isotopes of O₃ in the stratosphere exceeds their natural abundance, and the enrichment is nearly independent of mass (6). Valentini has interpreted the latter observation to indicate that the enrichment is caused by a symmetry effect in the dissociation of O₃ rather than by a normal kinetic isotope effect (67). He points out that the nonadiabatic transition involving crossing from the excited ¹Δ state of O₂ to the ground ³Σ state as the third O atom leaves can result in

Table 2. Ratio, *F*, of O₃ production rate by proposed mechanism to O₃ production rate by O₂ photolysis as a function of altitude as well as percentage increase in heavy O₃. The *J*_{O₃→³P}, [O₃], and *J*_{O₂} values are from (2). The [O₂] values are

0.21 times the total density taken from (7). The *R*₂₄₀ values are from (64) (see figure 4.35 for an overhead sun). The *F* values are fractional additional odd oxygen production rates relative to that produced by O₂ photodissociation.

Altitude (km)	<i>J</i> _{O₃→³P} (s ⁻¹)	[O ₃] (cm ⁻³)	<i>J</i> _{O₂} (s ⁻¹)	[O ₂] (cm ⁻³)	<i>R</i> ₂₄₀	<i>F</i>	Percentage
55	1.4 × 10 ⁻³	2.3 × 10 ¹⁰	1.1 × 10 ⁻⁹	2.4 × 10 ¹⁵	0.14	0.14	0.6
50	1.2 × 10 ⁻³	7.0 × 10 ¹⁰	8.0 × 10 ⁻¹⁰	4.5 × 10 ¹⁵	0.12	0.23	1.3
45	1.1 × 10 ⁻³	1.5 × 10 ¹¹	6.5 × 10 ⁻¹⁰	8.4 × 10 ¹⁵	0.11	0.27	1.9
40	8.0 × 10 ⁻⁴	5.8 × 10 ¹¹	3.7 × 10 ⁻¹⁰	1.7 × 10 ¹⁶	0.08	0.48	5.4

isotopic fractionation because there are twice as many ground state rotational levels available to an asymmetric O_2 product as to one in which both oxygens have mass 16 and zero nuclear spin. Despite having observed the effect of this symmetry on the rotational distribution of the $O_2(^1\Delta)$ product of O_3 dissociation, Valentini found it difficult to explain the stratospheric enrichment of heavy O_3 with the previously accepted dissociation mechanism. The reason for the difficulty is that the atomic oxygen product scrambles its isotopic label by interchange with O_2 more rapidly than it recombines to form O_3 .

The new dissociation mechanism discussed above, on the other hand, does provide a route to heavy O_3 enrichment: from the symmetry argument, O_3 with one heavy O atom has an increased probability of yielding triplet products, $O(^3P) + O_2(^3\Sigma)$, and some of these triplet dissociations yield O_2 with high enough vibrational energy to react with O_2 to form $O_3 + O$. Significantly, one of the original O_3 oxygens in this mechanism is incorporated directly into a new O_3 molecule without going through an O atom intermediate. Thus, the probability that a heavy O atom will remain in the O_3 pool is slightly increased above the random probability. Because O_3 is cycled by photodissociation many times (about 100 to 1700

times for altitudes from 55 to 35 km) before being destroyed by other processes (for example, $O + O_3 \rightarrow 2 O_2$), each of the cycles acts as a "plate" in a distillation column and causes a small amount of enrichment. A detailed account of the probabilities shows that the enrichment factor per cycle is given approximately by $E \approx [1 + (19f/3)] / [(1 + 2f)(1 + 4f)]$, where $f \equiv \Phi_3 R_{243} R_{v \geq 26}$. The overall enrichment factor for that fraction F of the O_3 produced by the new mechanism is E^{cycles} , where cycles is the number of O_3 photolysis events per O_3 destruction. The total percentage enrichment factor will then be $E_{tot} = \{1/(1 - F) + [F/(1 - F)](E^{cycles})\}$, so that the total percentage enrichment is $100(E_{tot} - 1)$. The last column of Table 2 shows that this value ranges from 0.6 to 5.4 percent for altitudes from 55 km to 40 km. Although the absolute magnitude and apparent altitude dependence from this simple analysis are not in agreement with observation (6), the new mechanism nonetheless predicts a substantial heavy O_3 enhancement and should be included in further models of this phenomenon.

The dynamics of O_3 photodissociation. We briefly speculate on a possible mechanism for production of such a strongly bimodal vibrational distribution. This bimodality implies two distinct dissociation

pathways for the $O(^3P) + O_2(^3\Sigma_g^-)$ channel. Either there are two different electronically excited states involved in the transition, or the initially prepared state possesses two entirely different routes to these products. The first possibility cannot be eliminated offhand; indeed, calculations find large transition moments for direct excitation to the repulsive surface which directly correlates to $O(^3P) + O_2(^3\Sigma_g^-)$ (68). However, the dominant source of ground-state products from Hartley band dissociation of O_3 is thought to involve nonadiabatic coupling of the initially prepared "B" (1^1B_2 in C_{2v} ; D^1A' in C_s) surface with this same repulsive surface correlating to ground-state products. If there are two distinct regions of intersection, then the corresponding product state distributions arising from flux through these different crossing regions may differ significantly. This phenomenon is observed in the photodissociation of ClO_2 and seen to lead to dramatic mode specificity in the photodissociation dynamics in that case (69, 70).

REFERENCES AND NOTES

- S. Chapman, *Q. J. R. Meteorol. Soc.* **3**, 103 (1930); *Philos. Mag.* **10**, 345 (1930).
- J. Eluszkiewicz and M. Allen, *J. Geophys. Res.* **98**, 1069 (1993).
- J. M. Price, J. A. Mack, C. A. Rogaski, A. M. Wodtke, *Chem. Phys.* **175**, 83 (1993).
- C. A. Rogaski, J. M. Price, J. A. Mack, A. M. Wodtke, *Geophys. Res. Lett.* **20**, 2885 (1993).
- M. Allen, *J. Geophys. Res.* **91**, 2844 (1986).
- See M. M. Abbas *et al.*, *J. Geophys. Res.* **92**, 13231 (1987), and references therein; J. A. Kaye, Ed., *Isotope Effects in Gas-Phase Chemistry*, vol. 502 of the ACS Symposium Series (American Chemical Society, Washington, DC, 1992), chaps. 1, 8 to 11, and 14.
- P. Warneck, *Chemistry of the Natural Atmosphere* (Academic Press, London, 1988).
- I. T. N. Jones and R. P. Wayne, *Proc. R. Soc. London A* **319**, 1452 (1974).
- K. H. Welge, *Can. J. Chem.* **52**, 1424 (1974).
- I. Arnold, F. J. Comes, G. K. Moortgat, *Chem. Phys.* **24**, 211 (1977).
- P. W. Fairchild and E. K. C. Lee, *Chem. Phys. Lett.* **60**, 36 (1978).
- C. E. Fairchild, E. J. Stone, G. M. Lawrence, *J. Chem. Phys.* **69**, 3632 (1978).
- S. T. Amimoto, A. P. Force, J. R. Wiesenfeld, *Chem. Phys. Lett.* **60**, 40 (1978).
- G. K. Moortgat and E. Kudzus, *Geophys. Res. Lett.* **5**, 191 (1978).
- J. C. Brock and R. T. Watson, *Chem. Phys. Lett.* **71**, 371 (1980).
- R. K. Sparks, L. R. Carlson, K. Shobatake, M. L. Kowalczyk, Y. T. Lee, *J. Chem. Phys.* **72**, 1401 (1980).
- S. T. Amimoto, A. P. Force, J. R. Wiesenfeld, R. H. Young, *J. Chem. Phys.* **73**, 1244 (1980).
- P. H. Wine and A. R. Ravishankara, *Chem. Phys.* **69**, 365 (1982).
- G. D. Greenblatt and J. R. Wiesenfeld, *J. Chem. Phys.* **78**, 4924 (1983).
- J. J. Valentini, D. P. Gerrity, D. L. Phillips, J.-C. Nieh, K. D. Tabor, *ibid.* **86**, 6745 (1987).
- M. Troler and J. R. Wiesenfeld, *J. Geophys. Res.* **93**, 7119 (1988).
- T. Kinugawa, T. Sato, T. Arikawa, Y. Matsumi, M. Kawasaki, *J. Chem. Phys.* **93**, 3289 (1990).
- A. A. Turnipseed, G. L. Vaghjiani, T. Gierczak, J. E. Thompson, A. R. Ravishankara, *ibid.* **95**, 3244 (1991).
- L. Froidevaux, M. Allen, Y. L. Yung, *J. Geophys. Res.* **90**, 12999 (1985).

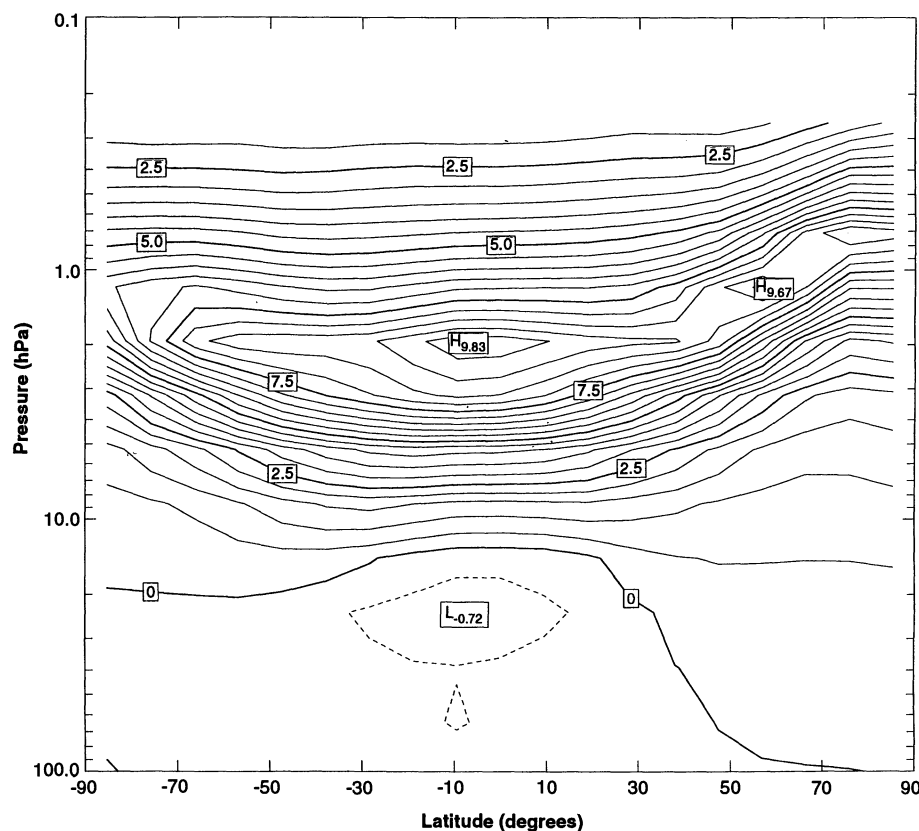


Fig. 5. Results from a 2D atmospheric model. Plotted is the percentage difference between a model with and without the new O_3 production mechanism. Altitude is given as effective pressure and negative latitude is the Southern Hemisphere. The results represent a 24-hour average.

25. R. T. Clancy, D. W. Rusch, R. J. Thomas, M. Allen, R. S. Eakman, *ibid.* **92**, 3067 (1987).
26. J. E. Frederick and R. J. Cicerone, *ibid.* **90**, 10733 (1985).
27. R. Simonaitis and M. T. Leu, *Geophys. Res. Lett.* **12**, 829 (1985).
28. R. P. Saxon and T. G. Slanger, *J. Geophys. Res.* **91**, 9877 (1986).
29. T. G. Slanger, L. E. Jusinski, G. Black, G. E. Gadd, *Science* **241**, 945 (1988).
30. H. Park and T. G. Slanger, *J. Chem. Phys.* **100**, 287 (1994).
31. R. Toumi, G. J. Kerridge, J. A. Pyle, *Nature* **351**, 217 (1991).
32. R. Toumi, *J. Atmos. Chem.* **15**, 69 (1992).
33. R. P. Wayne, *Atmos. Environ.* **21**, 1683 (1987).
34. A. Horowitz *et al.*, *J. Phys. Chem.* **92**, 4956 (1988).
35. A. G. Suits, R. L. Miller, L. S. Bontuyan, P. L. Houston, *J. Chem. Soc. Faraday Trans.* **89**, 1443 (1993).
36. L. S. Bontuyan, A. G. Suits, P. L. Houston, B. J. Whitaker, *J. Phys. Chem.* **97**, 6342 (1993).
37. The molecular beam pulse duration was 500 μ s. The nozzle diameter was 300 μ m. The nozzle to skimmer distance was 5 cm. The skimmer diameter was 500 μ m. The nozzle-to-laser beam distance was 17 cm.
38. The tunable UV radiation was produced by frequency doubling the output of an injection-seeded Nd:yttrium-aluminum-garnet (Nd:YAG)-pumped dye laser (Quanta-Ray DCR-4, PDL-1) and then summing the doubled light with the Nd:YAG fundamental. The linearly polarized laser beam (1- to 2-mJ pulse⁻¹, 0.35-cm⁻¹ bandwidth, and 10-ns pulses) was collimated with a telescope and focused into the molecular beam by a 7.5-cm focal length lens mounted inside the vacuum chamber.
39. W. C. Wiley and I. H. McLaren, *Rev. Sci. Instrum.* **26**, 1150 (1955).
40. Because of the large Doppler shift of the O(³P) fragments [calculated to be 1.77 cm⁻¹ for O(³P₂) at 5975 m s⁻¹], the frequency of the laser had to be scanned over the resonance to ensure that the entire velocity distribution was ionized while the image was being collected.
41. The total two-photon absorption cross section for the 3p \leftarrow 2p transition is independent of j ; D. J. Bamford, M. J. Dye, W. K. Bischel, *Phys. Rev. A* **26**, 3497 (1987).
42. Ozone for these experiments was prepared from dry O₂ with a commercial ozonator (Welsbach) and collected on silica gel in a trap immersed in a dry-ice/acetone slurry. The trapped O₃ was then pumped to remove O₃ decomposition products left over from the O₃ preparation process.
43. An excimer pumped dye laser (Lambda Physik, EMG201MSC/FL3002) frequency doubled in a β -barium borate crystal produced 1- to 3-mJ pulse⁻¹ in a 3-mm diameter spot.
44. LIF was accomplished with the visible output (560 to 400 nm) of a second excimer pumped dye laser (Lambda Physik, LPX205I/FL3002, 20-ns pulses, 1 to 10 mJ, 0.2-cm⁻¹ linewidth, and a 3-mm diameter spot size). The two counterpropagating laser pulses were spatially overlapped and temporally controlled with a delay generator (SRS DG535).
45. The angle θ is defined as that between the fragment recoil direction and the polarization vector of the incident light.
46. D. W. Chandler *et al.*, *J. Phys. Chem.* **94**, 4839 (1990).
47. D. J. DeRosier and A. Krug, *Nature* **217**, 130 (1968).
48. M. Zwick and E. Zeiler, *Optik* **38**, 550 (1973).
49. L. A. Schepp and B. F. Logan, *IEEE Trans. Nucl. Sci. NS-21*, 21 (1974).
50. K. R. Castleman, *Digital Image Processing* (Prentice-Hall, Englewood Cliffs, NJ, 1979).
51. Performing the inverse Abel transform on all rows of the projected image of Fig. 1 produces a 2D intensity profile that corresponds to a "slice" through the 3D velocity distribution containing the cylindrical axis of symmetry. The slice (not shown) also displays two pairs of lobes with an anisotropic angular distribution and can be represented as $I(v, \theta)$, where I is the intensity, v the speed (distance from the center), and θ the angle from the axis of symmetry. The speed distribution of Fig. 2 is then obtained by weighting each pixel in the slice by $(v \sin \theta)$ and integrating all intensity at a particular radius (speed).
52. Knowledge of the kinetic energy distribution of the O atom is enough to determine the total energy appearing in translation, because the O₂ kinetic energy can be determined by balancing linear momentum for the photodissociation event.
53. The power dependence of the 2+1 REMPI signal was measured for the O(³P₂) fragment and found to be quadratic, suggesting that the O₃ dissociation and O(³P₂) ionization steps were saturated.
54. K. Tonokura, N. Shafer, Y. Matsumi, M. Kawasaki, *J. Chem. Phys.* **95**, 3394 (1991).
55. The peak in the image corresponding to high internal energy is still present when a two-color photofragment imaging experiment is performed in which O atoms are again probed with 226-nm light but the O₃ is dissociated at longer wavelengths where the O₂(A³ Σ_u^+) and (A'³ Δ_u) states are inaccessible. This experiment suggests that the internal energy is not electronic [R. L. Miller, A. G. Suits, P. L. Houston, in preparation].
56. D. M. Creek and R. W. Nichols, *Proc. R. Soc. London Ser. A* **341**, 517 (1975).
57. W. B. DeMore *et al.*, *Jet Propulsion Lab Publ. No. 92-20* (1992).
58. R. Harris, M. Blackledge, J. Generosa, *J. Mol. Spectrosc.* **30**, 506 (1969).
59. P. C. Cosby, H. Park, R. A. Copeland, T. G. Slanger, *J. Chem. Phys.* **98**, 5117 (1993).
60. G. D. Billing and R. E. Kolesnick, *Chem. Phys. Lett.* **200**, 382 (1992).
61. M. J. Daniels and J. R. Wiesenfeld, *J. Chem. Phys.* **98**, 321 (1993).
62. Although the product imaging experiment predicts that $v = 27$ is more populated than $v = 26$, attempts to observe $v = 27$ directly by LIF were unsuccessful. LIF detection of $v = 26$ was already quite difficult; the spectrum of Fig. 3 required substantial signal averaging and is the average of four 30-min scans. Detection of $v = 27$ is expected to yield about four times less signal because of the smaller Franck-Condon factors in the probe step. There is also more scattered light background when the probe laser is tuned to detect $v = 27$. In addition, we made no attempt to determine how much O₂ might be present in the O₃ trap over which N₂ flowed to the reaction cell. If appreciable O₂ impurity is present in the nominal O₂/N₂ mixture, then O₂($v = 27$) might have a short enough lifetime to largely disappear by the time the probe laser is fired. In any event, it is unlikely that the striking agreement between $v = 19$ and 26 (shown in Fig. 2) suddenly diverges at $v = 27$. Taken together, the two experiments leave room for only one interpretation: O₃ photolysis at 226 nm leads to a bimodal vibrational distribution in the O₂ photoproduct with one peak near $v = 14$ and the second at $v = 27$.
63. This quantity denotes the wavelength-integrated photolysis rate for O₂.
64. G. Brasseur and S. Solomon, *Aeronomy of the Middle Atmosphere* (Reidel, Dordrecht, Netherlands, 1984).
65. R. Toumi, S. Bekki, R. J. Cox, *J. Atmos. Chem.* **16**, 135 (1993).
66. Note that 1 hPa = 1 mbar.
67. J. J. Valentini, *J. Chem. Phys.* **86**, 6757 (1987).
68. A. Banichevich, S. D. Peyerimhoff, F. Grein, *Chem. Phys.* **178**, 155 (1993).
69. H. F. Davis and Y. T. Lee, *J. Phys. Chem.* **96**, 5681 (1992).
70. K. A. Peterson and H. J. Werner, *ibid.*, p. 8948.
71. The work at Cornell was supported by the National Science Foundation (NSF) under grant CHE-9224432. We are grateful to S. Rogers for help in obtaining some of the imaging data. The work at UCSB was supported by NSF grants ATM-8922214, CHE-8957978, CHE-8411302, a Camille and Henry Dreyfus Foundation Teacher Scholar Award (A.M.W.), and an Alfred P. Sloan Foundation Research Fellowship (A.M.W.).

8 April 1994; accepted 8 August 1994